Fuel 240 (2019) 75–83

Contents lists available at ScienceDirect

Fuel

journal homepage: www.elsevier.com/locate/fuel

Full Length Article

Fully-resolved simulations of coal particle combustion using a detailed multi-step approach for heterogeneous kinetics

G.L. Tufano[a], O.T. Stein[a,*], A. Kronenburg[a], G. Gentile[b], A. Stagni[b], A. Frassoldati[b], T. Faravelli[b], A.M. Kempf[c], M. Vascellari[d], C. Hasse[e]

[a] Institut für Technische Verbrennung, Universität Stuttgart, Herdweg 51, 70174, Germany
[b] Dipartimento di Chimica, Materiali e Ingegneria Chimica, Politecnico di Milano, Piazza L. da Vinci, 32, 20133 Milano, Italy
[c] Institute for Combustion and Gasdynamics (IVG), Chair for Fluid Dynamics, University of Duisburg-Essen, 47057, Germany
[d] Numerical Thermo-Fluid Dynamics, TU Bergakademie Freiberg, Fuchsmühlenweg 9, Freiberg 09599, Germany
[e] Simulation of Reactive Thermo-Fluid Systems, TU Darmstadt, Otto-Berndt-Straße 2, Darmstadt 64827, Germany

ARTICLE INFO

Keywords:
DNS
LES
Pulverized coal particle
Porous media
Detailed heterogeneous kinetics

ABSTRACT

Fully-resolved simulations of the heating, ignition, volatile flame combustion and char conversion of single coal particles in convective gas environments are conducted and compared to experimental data (Molina and Shaddix, 2007). This work extends a previous computational study (Tufano et al., 2016) by adding a significant level of model fidelity and generality, in particular with regard to the particle interior description and heterogeneous kinetics. The model considers the elemental analysis of the given coal and interpolates its properties by linear superposition of a set of reference coals. The improved model description alleviates previously made assumptions of single-step pyrolysis, fixed volatile composition and simplified particle interior properties, and it allows for the consideration of char conversion. The results show that the burning behavior is affected by the oxygen concentration, i.e. for enhanced oxygen levels ignition occurs in a single step, whereas decreasing the oxygen content leads to a two-stage ignition process. Char conversion becomes dominant once the volatiles have been depleted, but also causes noticeable deviations of temperature, released mass, and overall particle conversion during devolatilization already, indicating an overlap of the two stages of coal conversion which are usually considered to be consecutive. The complex pyrolysis model leads to non-monotonous profiles of the combustion quantities which introduce a minor dependency of the ignition delay time τ_{ign} on its definition. Regardless of the chosen extraction method, the simulations capture the measured values of τ_{ign} very well.

1. Introduction

Pulverized coal combustion (PCC) is a major technology for thermal energy conversion, particularly for providing base load power. It is, however, crucial for a sustainable future of coal conversion that pollutants from coal are heavily reduced and climate change is mitigated. To achieve any kind of significant progress detailed insights in the underlying physical and chemical processes that govern PCC are required. A fundamental understanding of the principal processes can be obtained by state-of-the-art experimental investigations [1–5] and by performing detailed numerical simulations. As the flow conditions in PCC furnaces are typically turbulent, the large eddy simulation (LES) approach is increasingly employed for capturing the highly transient processes in pulverized coal flames [6–17]. However, LES does not resolve the smallest scales of the process, but requires detailed sub-grid closures for effects that occur on the level of individual particles or small particle ensembles. Such closures can be derived from resolved simulation approaches, i.e. resolved laminar flow simulations (RLS) and direct numerical simulations (DNS). Typically, these simulation approaches resolve all scales of turbulence and the bulk flow, but do not consider the fluid boundary layers right at the particle surface and consider Lagrangian point particles instead [18–27], whereas the Arbitrary Lagrangian–Eulerian (ALE) method was employed in [28]. The number of simulations that fully resolve the particle boundary layers is scarce and primarily one- and two-dimensional setups have been considered [29–32]. Previous studies by the present authors considered fully-resolved simulations of coal particle ignition and volatile flame burning of single coal particles in laminar flow [33–35] and of coal particle ensembles in both laminar and turbulent convective environments [36,37]. Our previous simulations required limiting -albeit

* Corresponding author.
E-mail address: o.stein@itv.uni-stuttgart.de (O.T. Stein).

https://doi.org/10.1016/j.fuel.2018.11.139
Received 11 June 2018; Received in revised form 23 November 2018; Accepted 27 November 2018

reasonable- assumptions such as pre-fitted single-step devolatilization and a fixed (presumed) volatile composition based on relatively small hydrocarbons. Furthermore, a simplified description of the particle interior processes was assumed and the effects of porosity and char conversion were omitted from the analysis. The present work alleviates the previous limitations by

- considering a detailed kinetic model for the heterogeneous particle processes that dynamically predicts the volatile release rate and composition, including large hydrocarbons
- including a detailed description of the particle interior properties such as porosity and particle-internal fluid flow
- accounting for char conversion.

The remainder of the paper is structured as follows: The modeling approach is detailed in Sec. 2, which is followed by a description of the computational setup and the reference experiments in Sec. 3, the results in Sec. 4 and conclusions in Sec. 5.

2. Modeling

Our simulation approach fully resolves the flow, mixing and reaction processes in the gas phase on the exterior of the solid fuel particle, similar to our previous model implementation [34,36,37]. However, the particle interior description is significantly improved compared to previous work, by considering the gas-solid interaction processes inside the particle using a sophisticated model for porous media with chemical reactions [38–40].

2.1. Mathematical model

We distinguish between our model description of the particle interior and exterior. The particle is considered as a porous medium bounded by a spherical outer shell that separates it from the exterior gas phase. To describe the exterior gas the conservation equations of momentum, enthalpy, total and species mass in their variable density formulation are solved as previously presented in [34] and omitted here for brevity. Pressure-velocity (and -density) coupling is performed using OpenFOAM's *hybrid approach* [41]. The particle interior volume is split into a gas (superscript ^{G}) and solid (superscript ^{S}) contribution, where the gas and solid volumes can be calculated from the porosity ϵ

$$V^G = V_{sphere} \cdot \epsilon \tag{1}$$

$$V^S = V_{sphere} \cdot (1 - \epsilon) \tag{2}$$

and $V_{sphere} = V^G + V^S$. Total and individual species mass conservation is considered for the particle interior *solid phase* as

$$\frac{\partial[\rho^S(1-\epsilon)]}{\partial t} = \sum_{i=1}^{N^S} \dot{\omega}_i^S \tag{3}$$

$$\frac{\partial[\rho^S(1-\epsilon)Y_i^S]}{\partial t} = \dot{\omega}_i^S, \tag{4}$$

with time t, density ρ, reaction rate $\dot{\omega}$, number of species N and species mass fraction Y. Similarly, for the particle interior *gas phase* we write

$$\frac{\partial(\rho^G \epsilon)}{\partial t} + \nabla\cdot(\rho^G \mathbf{U}) = \sum_{j=1}^{N^G} \dot{\omega}_j^G \tag{5}$$

$$\frac{\partial(\rho^G \epsilon Y_j^G)}{\partial t} + \nabla\cdot(\rho^G Y_j^G \mathbf{U}) = -\nabla\cdot(\rho^G Y_j^G \mathbf{v_j^c}) + \dot{\omega}_j^G, \tag{6}$$

with the local density of the gas enclosed inside the particle ρ^G (varying with the ideal gas law), the local superficial velocity $\mathbf{U}$ [42] and the correction diffusion velocities $\mathbf{v_j^c}$. Note that the subscripts $_i$ and $_j$ have been used to distinguish between solid and fluid species. The correction diffusion velocities are introduced to enforce mass conservation according to [43]

$$\mathbf{v_j^c} = \mathbf{v_j} + \mathbf{v^c} \tag{7}$$

$$\mathbf{v_j} = -\frac{D_{eff,j}}{Y_j^G}\nabla Y_j^G \tag{8}$$

$$\mathbf{v^c} = -\sum_{j=1}^{N^G} \mathbf{v_j}, \tag{9}$$

where $\mathbf{v_j}$ includes both bulk and pore diffusion by considering an effective diffusion coefficient $D_{eff,j}$ and $\mathbf{v^c}$ is a velocity correction factor as introduced in [38]. The momentum conservation equation for the particle interior gas phase reads

$$\frac{\partial \rho^G \epsilon \mathbf{U}}{\partial t} + \nabla\cdot(\rho^G \mathbf{U}\mathbf{U}) = -\nabla p + \nabla\cdot\tau + \rho^G \mathbf{g} + \mathbf{S}, \tag{10}$$

with pressure p, gravity vector $\mathbf{g}$ and

$$\tau = \mu^G\left[\nabla\mathbf{U} + (\nabla\mathbf{U})^T - \frac{2}{3}(\nabla\cdot\mathbf{U})\mathbf{I}\right], \tag{11}$$

where μ denotes dynamic viscosity. The momentum source term for porous media $\mathbf{S}$ in Eq. (10) is calculated according to the Darcy-Forchheimer law

$$\mathbf{S} = -\left(\mu\mathbf{Da} + \frac{1}{2}\rho^G|u_{kk}|\mathbf{F}\right)\mathbf{U} \tag{12}$$

and affects the pressure drop inside the particle by means of a viscous and an inertial contribution, which are characterized by the Darcy **Da** and Forchheimer **F** tensors, respectively. Due to the low particle Reynolds numbers considered here the inertial contribution is ignored [38]. **Da** represents the resistance against the flow of gas produced inside the porous medium, which enhances the intra-particle pressure gradients. Ranzi et al. [44] reported how the full momentum equations (Eq. 10) can be simplified under the assumptions of steady-state and very low flow velocity, obtaining the widely used Darcy law for porous media. Here we employ the more general approach to characterize the evolution of a solid fuel particle, which is governed by the fundamental conservation equations of mass, momentum, and energy, and accounts for porous media effects via porosity and Darcy-Forchheimer source terms. Particle interior heat transfer occurs by conduction and (gas) convection. The amount of gas instantaneously contained inside the particle pores is limited and, considering the very large surface area of the porous medium, it is reasonable to consider that the gas instantaneously reaches the temperature of the solid. This assumption does not imply that the particle internal thermal gradients are neglected, but only that locally the temperature of the solid and the gas contained inside the pores is the same. In fact, the heat capacity $\rho^S c_p^S$ of the solid is much larger than that of the gas formed inside the particle. Thus, local thermal equilibrium is assumed between the co-existing solid and gas phase and a unique temperature field for the porous medium is obtained solving the equation

$$c_p^G\frac{\partial(\rho^G \epsilon T)}{\partial t} + c_p^G\nabla\cdot(\rho^G \mathbf{U}T) + c_p^S\frac{\partial[\rho^S(1-\epsilon)T]}{\partial t} = \nabla\cdot(\lambda_{eff}\nabla T) + \dot{Q}_R, \tag{13}$$

with temperature T, heat capacity c_p, effective thermal conductivity λ_{eff} and heat release by chemical reaction $\dot{Q}_R$. The density of the gas mixture ρ^G is calculated from the perfect gas law and all other transport properties are evaluated by applying the mixture averaging rules [45].

2.2. Boundary conditions

A set of boundary conditions at the (spherical) interface between the particle interior and exterior needs to be applied. Atmospheric conditions for total pressure and the equivalence of the convective fluxes at

both sides of the interface are enforced. Zero-gradient conditions for the solid species mass fractions are assumed. The gaseous species mass fractions and temperature need to satisfy the following equivalence of fluxes at both sides of the interface

$$\rho^G D_{eff,j} \frac{\partial Y_j^G}{\partial r}\bigg|_{int} = \rho^G D_j \frac{\partial Y_j^G}{\partial r}\bigg|_{ext} \tag{14}$$

$$\lambda_{eff} \frac{\partial T}{\partial r}\bigg|_{\text{int}} = \lambda \frac{\partial T}{\partial r}\bigg|_{\text{ext}} + Q_{r,p}, \quad \text{with} \quad Q_{r,p} = -\frac{\varepsilon_p}{2(2-\varepsilon_p)}(4\sigma T_p^4 - G_p) \tag{15}$$

where $Q_{r,p}$ is the surface radiative heat flux, ε_p the particle emissivity, σ the Stefan-Boltzmann constant and G the incident radiation. As discussed in [36], a sensitivity study within the full range $0 \leqslant \varepsilon_p \leq 1.0$ did not reveal any significant influence for particle configurations similar to the one considered here. Moreover, we have conducted test runs including $Q_{r,p}$ and did not find any significant role of it for ignition since, up to the ignition point, temperature levels in the particle vicinity are comparatively low. After ignition, radiative effects become more important, especially in the presence of heterogeneous chemistry, but since the comparison with the experimental measurement is attempted here only for ignition delay but no reference data is available for the subsequent combustion phase, the term $Q_{r,p}$ in Eq. (15) has been omitted from the present DNS. Gas phase radiation is included by the P1-approximation [46,47], using absorption and emission coefficients for the continuous phase. By imposing the equivalence of the convective fluxes across the interface, the convective contributions on both sides cancel out, and therefore do not directly appear in Eqs. (14) and (15). A reaction source term, is also not included in Eqs. (14) and (15), since reactions do not occur on the surface, but are purely volume-based instead.

2.3. Physical properties

The thermophysical and transport properties of all species involved in the conversion process are obtained from established databases [48], and interpreted via the OpenSMOKE++ library [49] as previously reported in [38,40]. Due to the limited availability of experimental data regarding the heat capacity, thermal and (effective) mass diffusivity of the solid phase, simple models are assumed here. The heat capacity c_p^S of the solid species contained in the coal is assumed to be constant and equal to the nominal value for the coal of interest. The effective thermal conductivity λ_{eff} of the porous medium is obtained as a linear combination of the gas and solid contributions

$$\lambda_{eff} = \epsilon\, \lambda^G + (1-\epsilon)\lambda^S, \tag{16}$$

where for λ^S the nominal value of the given coal is considered. The effective pore diffusion coefficients are evaluated as in [39]

$$D_{eff,j} = \left[\frac{1}{D_j^m} + \frac{1}{D_j^{Kn}}\right]^{-1} \cdot \frac{\epsilon}{\tau^2}, \tag{17}$$

where D_j^m and D_j^{Kn} are the molecular and Knudsen diffusivities and τ is the local tortuosity. The Knudsen diffusivity is calculated as

$$D_j^{Kn} = \frac{d_{por}}{3}\sqrt{\frac{8RT}{\pi M_j}}, \tag{18}$$

with the mean pore diameter $d_{por} = 0.3\,\mu m$ as estimated in [39] for bituminous coal, the universal gas constant R and molar species mass M.

During pyrolysis the solid particle undergoes radical changes of its internal structure due to drying, devolatilization and char conversion. We have conducted a pyrolysis regime analysis based on Biot and Pyrolysis numbers according to Paulsen et al. [50] for the present case. For the sake of simplicity, the rate of the initial decomposition of reference COAL1 (see Section 2.4) was used as being representative of coal pyrolysis. The analysis revealed that the pyrolysis regime for the present case is *kinetically-limited isothermal*, but very close to the boundary of the region where internal temperature gradients begin to become important. In the *kinetically-limited isothermal* regime a thermally thin particle has limited internal temperature gradients during pyrolysis and the chemical reactions take place uniformly throughout its volume. For these conditions the mass loss results in an increase of the porosity ϵ without variations of the particle size [38]. This assumption is sufficiently robust in the case of coal particles which are subjected to modest shrinking during devolatilization. Therefore we include mass loss by assuming a linear increase of the particle porosity ϵ with particle conversion χ [39]

$$\chi = 1 - \frac{m^S}{m_0^S} \tag{19}$$

$$\epsilon = \epsilon_0 + \chi(1-\epsilon_0), \tag{20}$$

where m^S and m_0^S are the current and initial mass of the solid phase and ϵ_0 is the initial porosity. The solid mass varies according to:

$$\frac{dm^S}{dt} = \sum_{i=1}^{N^S} \dot{\omega}_i^S V^S \tag{21}$$

Conversely the tortuosity decreases linearly with particle conversion [39]

$$\tau = \tau_0 - \chi(\tau_0 - 1). \tag{22}$$

2.4. Kinetic model

A predictive, multi-step kinetic model for coal pyrolysis [51] and char conversion [39] is applied. The model is able to predict the thermal degradation of different coals across a wide range of operating conditions only requiring the elemental composition of the coal. While the physical properties are assigned to the coal as a whole, the chemical-kinetic properties of the coal of interest for a given problem are obtained by linear interpolation of the kinetic properties of three reference coals, i.e. three separate species evolving simultaneously. Here, we consider Pittsburgh seam high-volatile bituminous coal the properties of which are given in Table 1. Table 2 shows its composition in terms of the reference coals COAL1, COAL2 and COAL3 defined in [51].

The kinetic sub-mechanism describing the pyrolysis of the reference coals is based on the previous work of Sommariva et al. [51] and composed of 32 species and 36 reactions. The sub-mechanism for heterogeneous char reactions considers char combustion, char gasification and thermal annealing in a set of 8 species and 14 reactions with rates and heats of reaction based on the work of Maffei et al. [39]. The latter represents a volume-based approach. For the sake of simplicity, even the gasification reactions are volume-based as already pointed-out in [39]. The model also accounts for particle drying by means of a single kinetic rate law. The heterogeneous mechanisms are made available as Supplementary material. The volatile matter released during pyrolysis is a complex mixture of light gases and heavy tars, the latter of which are modeled as lumped species [51]. According to the different molecular structure and atomic composition, each of the lumped tar species released during coal devolatilization is split up into a limited number of

Table 1
Proximate and ultimate analysis (as received) of Pittsburgh seam high-volatile bituminous coal [2].

Proximate analysis		Ultimate analysis	
Volatile matter	35.89	C	75.23
Fixed carbon	56.46	H	5.16
Moisture	0.47	O	9.83
Ash	6.95	N	1.43
HHV	30.94 MJ/kg	S	2.00

Table 2
Reference coal distribution for the Pittsburgh bituminous coal [mass%].

COAL1	COAL2	COAL3	ASH
27.90	49.41	12.69	10.00

Table 3
Assignment of the lumped tar species from [51] to hydrocarbon species in the gas phase mechanism [mass%].

VTAR1	25.8 $C_{10}H_{12}$ + 74.2 $C_{12}H_8$
VTAR2	22.4 $C_{10}H_7CH_3$ + 50.8 $C_{20}H_{10}$ + 26.8 $C_{11}H_{12}O_4$
VTAR3	9.7 $C_{10}H_7CH_3$ + 22.1 $C_{20}H_{10}$ + 27.3 $C_9H_{10}O_2$ + 40.8 $C_{11}H_{12}O_4$
BTX2	41.8 $C_{10}H_7CH_3$ + 58.2 $C_{10}H_{12}$

compounds already available inside the detailed kinetic mechanism for the gas phase. Aromatic and oxygenated aromatic species are adopted: Methyl-naphthalene, Tetralin, Acenaphthylene, Coumaryl, Sinapaldehyde and a large PAH species, see Table 3. These species are selected in order to have the same chemical functionalities of the original tar species and their relative amount is calculated by solving a linear system representing the conservation of C, H, O atomic balances.

Finally, the homogeneous gas-phase kinetics are described by using the POLIMI kinetic model (version 1407 [52,53]): It describes the pyrolysis and oxidation of hydrocarbons up to C_{16}, as well as the formation paths of major pollutant species. To limit the computing demand of the fully-resolved simulation, the complete mechanism was reduced following the multi-step algorithm, based on flux and sensitivity analysis, implemented in the DoctorSMOKE++ software [54], which led to a final skeletal scheme with 76 species and 973 homogeneous reactions. The homogeneous reaction scheme is made available as Supplementary material of this work as well.

2.5. Model fidelity

It shall be noted here that the modelling approach described in this Sec. 2 is relatively complex and that simpler model descriptions may suffice to recover experimental particle ignition delay times [34]. However, as will be seen from Fig. 4 in the results section, when moving from the particle core to its outer layers, while temperature is mostly uniform, temperature differences of up to 400 K may be encountered near the surface. Therefore it seems reasonable to neglect particle shrinking since the reactions occur throughout the entire particle volume, leading to an increase in particle porosity at constant particle diameter, cf. Sec. 2.3. Yet, significant temperature and oxygen gradients (Fig. 4) can establish inside the particle and have an impact on the homogeneous and heterogeneous burning behavior. Therefore we consider the introduced model complication fundamental for accurately modeling the physico-chemical phenomena occurring in- and outside the particle for the present conditions (particle diameter $d_p = 0.1$ mm) already. However, we would expect even bigger effects for larger particles, giving stronger incentives for the higher CPU cost of the present model compared with simpler models.

3. Experimental and computational setup

3.1. Reference experiments

Molina & Shaddix [2] evaluated the effect of enhanced O_2 levels and the presence of CO_2 on the ignition delay of Pittsburgh seam high-volatile bituminous coal particles. Particles with a mean diameter of 0.1 mm were injected in the laminar flow of various mixtures of hot combustion products from a Hencken burner as reported in Table 4. Due to the very slow coal supply (0.02 g/min) the experimentalists argued that particle interactions are negligible and single-particle ignition and combustion events occurred. The ignition delay time of the solid particles was evaluated from ensemble-averaged images of the experimental CH^* chemiluminescence.

Table 4
Experimental balance gas compositions (mol%) [2].

Case	N_2-21	N_2-30	CO_2-21	CO_2-30
O_2	21.00	30.00	21.00	30.00
N_2	65.08	56.00	0.00	0.00
CO_2	1.65	1.65	65.31	57.02
H_2O	12.27	12.34	13.69	12.98

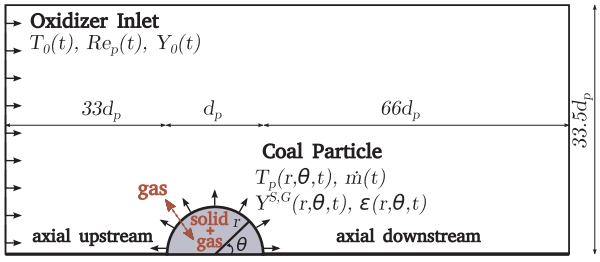

Fig. 1. Computational domain for the RLS.

3.2. Numerical setup

The computational setup considered here extends the one previously reported in [34]. Fig. 1 shows the two-dimensional, axisymmetric, multi-region domain, which is 100 particle diameters ($d_p = 0.1$ mm) long, 33.5 d_p wide and set up as a 5° wedge, as rotational symmetry in laminar flow has been assumed. Based on our previous grid analyses [34] the boundary layer around the particle is fully resolved with 20 cells in the radial and more than 70 cells in the circumferential direction, with a characteristic cell width of $0.02d_p$ both in the external gas phase and in the particle interior. The envelope flame is also resolved with at least 20 cells. At the left boundary of the domain, mixtures of hot combustion products, cf. Tab. 4, are introduced as transient boundary conditions. These transient BCs are obtained from auxiliary Euler-Lagrange simulations of the Hencken burner (not shown for brevity), which result in time-varying oxidizer temperatures $T_0(t)$ and particle Reynolds numbers $\mathrm{Re}_p = v_{rel}\, d_p/\nu = f(t)$, as presented in Fig. 2 of [34]. The initial values from the auxiliary simulations are also used to initialize the (particle exterior) computational domain for the fully-resolved simulation and the actual value of the transient $T_0(t)$ reaches the particle surface in less than 5 ms. Since after about 15 ms, $T_0(t)$ has already reached an asymptotic value, this delay does not affect the ignition delay time predicted for the particles. For the solid coal particle $\rho^S = 1400\,\mathrm{kg/m^3}$, $c_p^S = 1680\,\mathrm{J/(kg\cdot K)}$ and $\lambda^S = 0.3\,\mathrm{W/(m\cdot K)}$ are considered. As reported in [39], the heat of pyrolysis is less than 1% of the combustion heat and has therefore been neglected, whereas the heats of the heterogeneous reactions are calculated, considering the enthalpy of formation of the gas species only [39]. The initial particle porosity and tortuosity are set to $\epsilon_0 = 25\%$ and $\tau_0 = \sqrt{2}$ as estimated in [39]. The initial particle temperature T_p^0 is set to 350 K after performing sensitivity analyses using the Euler-Lagrange set-up, exploring the effects of different boundary conditions at the furnace inlet. This T_p^0 is lower than the one previously reported in [34] where a significant particle pre-heat was assumed and a parameter study of T_p^0 was shown. However, the present Euler–Lagrange simulations predict a significantly smaller pre-heat and $T_p^0 = 350$ K is considered for all cases.

The simulations are performed with a solver based on OpenFOAM v2.4.x after coupling it with the *OpenSMOKE++* library. Note again that different sets of equations are solved in different areas of the multi-region domain: The standard gas phase conservation equations are solved for the particle exterior, while the complex intra-particle two-phase model described in Section 2 is solved for the particle interior

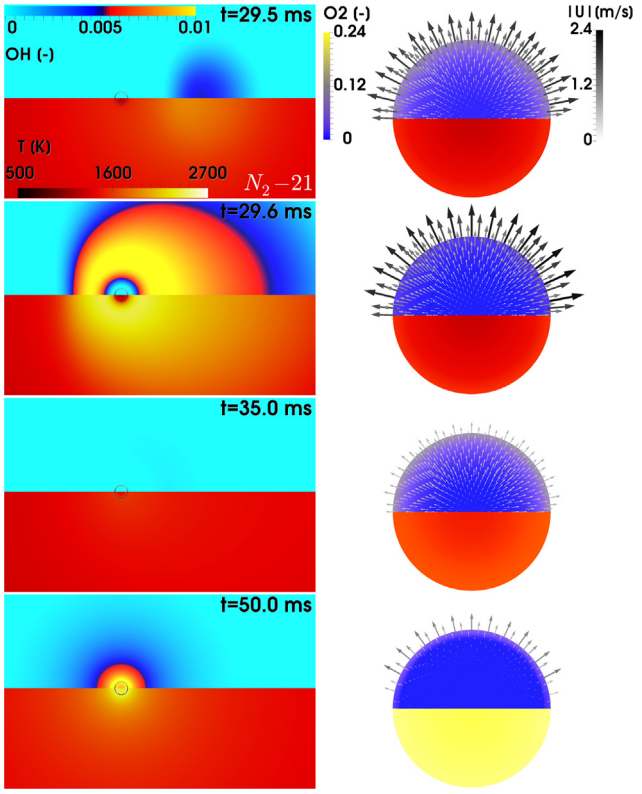

Fig. 2. Selected time instants during ignition and combustion of a coal particle immersed in the N_2-21 mixture, where the particle surface is marked by a circle. Left: Mass fraction Y_{OH} (top frames) and temperature (bottom frames) contours *in the vicinity* of the particle, Right: Velocity vectors colored by magnitude, mass fraction Y_{O_2} (top frames) and temperature (bottom frames) contours for the *particle interior*. (For interpretation of the references to color in this figure, the reader is referred to the web version of this article.).

(grey area in Fig. 1). A variable time step is used and a Courant number Co$\leqslant$ 0.5 is enforced for stability and accuracy in all simulations. The chemistry solver is subject to further sub-stepping and not affected by Co. Simulations are typically run on 24/48/64 Xeon/Opteron cores, requiring about 20 h of wall time to reach ignition and up to 200 h until the 60 ms of physical time presented here are simulated.

4. Results

The sequence of ignition and burning of the coal particle is illustrated in Fig. 2, where the experimental condition N_2-21 of [2] is chosen as a representative example for all cases from Table 4. After an initial stage of particle heat-up that triggers the volatile matter release from the particle to the surroundings (not shown), homogeneous gas phase ignition occurs at 29.5 ms, as indicated by the significant amounts of OH and elevated temperature that can first be observed in the particle wake (29.5 ms) and which quickly envelope the entire particle (29.6 ms). Up to this point the ignition sequence is identical to the one described for our earlier simpler model, which did not account for the particle interior flow, was based on a single-step pyrolysis model and neglected char conversion. In that case, the envelope flame would continue to burn continuously at a small stand-off distance from the particle and extinguish after volatile depletion [34]. However, with the present detailed porous-media model that includes char conversion a significantly different burning behavior is found. After ignition the volatile flame immediately consumes the light volatile gases available in the vicinity of the particle, whereas more time is required for the decomposition of the heavy tars. In addition, as more volatiles are produced inside the particle, they need to overcome the resistance of the porous medium before they can be released to the particle exterior gas phase. This effect is particularly strong for the heavy tar species, which are transported through the particle pores more slowly. This delay causes the flame to slowly lose combustion intensity and the peak OH mass fractions and temperature observed at 29.6 ms start to decrease until no elevated Y_{OH} and temperature indicative of a flame remain, see Fig. 2 (35 ms). After this, due to the ongoing release of volatile matter and the decomposition of the large tars between 30 and 35 ms, chemical reactions occur right at the particle surface and start to form further OH and to increase temperature again. From this moment onwards, the heterogeneous char reactions promote the formation of chemical species and heat release at the particle surface. The mass and heat provided at the surface diffuse away, both towards the surrounding gas phase and into the particle interior, forming an extended circular region around the particle where chemical conversion occurs. This region continues to expand radially with its largest extent (roughly 1.5 particle diameters as judged by the OH contour) shown in Fig. 2 (50 ms, left). After 50 ms chemical reactions continuously reduce in intensity until no OH is left and the temperature field reduces to the single value of the furnace temperature (not shown), which indicates the end of the conversion process. On the right of Fig. 2 the O_2 mass fraction, temperature and velocity vectors in the particle interior for the same time instants are shown. It can be observed that ignition occurs when the particle temperature is approximately the same as the one of the surrounding gas phase and during a phase of high mass release (peak velocities of 2.4 m/s) from the particle. During the subsequent phase of cool-down and radical depletion in the initial volatile flame the mass release from the particle decreases, while the particle is mildly heated by its (still hotter) surroundings. After 35 ms the secondary (surface) ignition event happens, this time due to the heterogeneous conversion of the char, which leads to a continuous heat-up of the particle and again increased levels of mass release from the particle as shown in Fig. 2 (50 ms, right). Since the velocity vectors shown in Fig. 2 represent the rate of overall mass release from the particle (irrespective of its nature of production) a closer look into the mass release contributions due to pyrolysis and char conversion is taken. Figure 3 shows the temporal evolution of (volume-averages of) some selected species in the particle interior. For ease of discussion the complex set of species from the detailed pyrolysis and char conversion model has been reduced to show the three reference coals, the overall mass of char, three selected light gas species (CO, CO_2 and O_2) and the sum of all tar species only. To judge the relative contributions from pyrolysis and char conversion, simulations with (solid lines) and without char reactions (dashed lines) are compared and case N_2-30 is chosen, as its elevated oxygen levels trigger more char conversion than the reference case N_2-21. During the first 20 ms the composition of the solid coal, Fig. 3 (left), remains unchanged since the particle has not yet reached a sufficiently high temperature. From 20 ms on devolatilization starts and reference coals COAL2 (representing bituminous coal) and COAL3 (lignitic coal) are rapidly consumed to produce more of COAL1 (hydrogen-rich coal), as well as volatile gases, tars and char. Between 23 and 30 ms COAL1 is also consumed, while further char is formed. Up to around 33 ms the curves from the simulations with and without char conversion completely overlap, while the simulation with char consumption continuously reduces the char mass after that, while it stays constant if char conversion is neglected.

The (complex) time evolution of the gaseous species in the particle interior is shown in Fig. 3 (bottom). During the early stages (not shown) the gas from the surrounding fluid phase rapidly diffuses through the pores inside the particle as O_2 and CO_2 have reached the nominal concentration of the external mixture by 10 ms. Once the depletion of the reference coals begins, both light gas species such as CO and CO_2 and heavier tars are produced by pyrolysis and first released to the particle interior, before being ejected from the particle to the exterior gas phase, alongside the O_2 enclosed in the pores. As the (large) tar species are only formed during pyrolysis and subsequently depleted

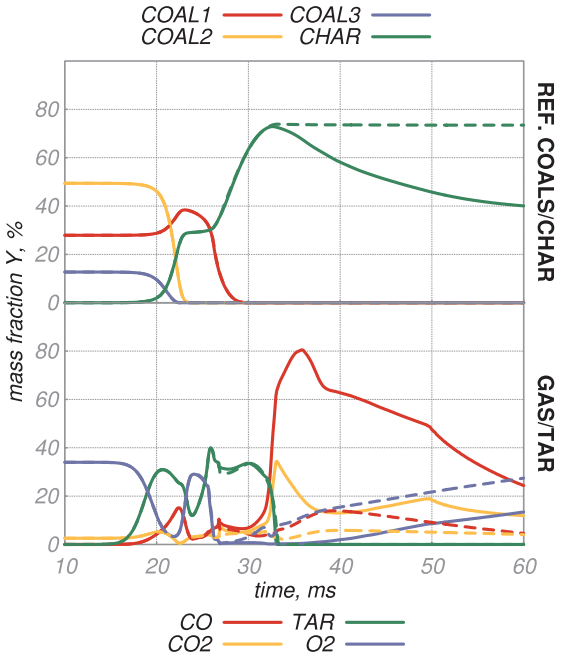

Fig. 3. Temporal evolution of the particle interior fields, reference coals and char (top), selected volatile species and tars (bottom) for case N_2-30. Each line represents the volume-average of the distribution in the resolved particle interior. CO, CO_2 and O_2 are taken as representative species from the gas mixture and *char* and *tar* represent the sum of the complex mixture of various char and tar (cf. Tab. 3) species present in the detailed pyrolysis/char conversion submodel. The dashed lines refer to an identical simulation, but with char conversion switched off. (For interpretation of the references to color in this figure, the reader is referred to the web version of this article.).

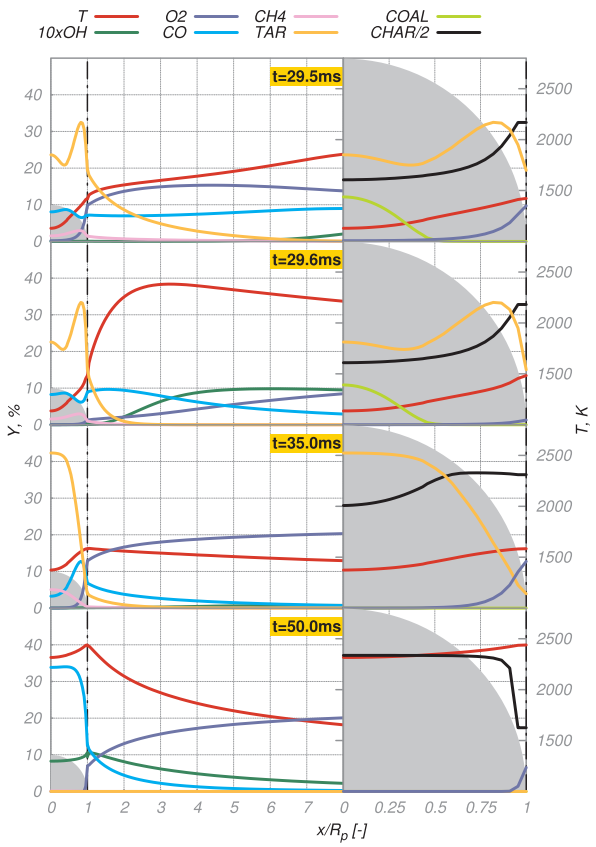

Fig. 4. Downstream centerline profiles of temperature and main chemical species for case N_2-21, extracted at the same time instants selected for Fig. 2 (left). On the right selected profiles are zoomed into better illustrate their distribution inside the particle. (For interpretation of the references to color in this figure, the reader is referred to the web version of this article.).

they are only present in the particle interior until the end of pyrolysis (33 ms). In contrast, CO and CO_2 can be formed by char oxidation and are therefore present inside the particle at even later stages of the conversion process, while O_2 is consumed and stays near zero between 25 and 35 ms for the case with char conversion. With char conversion switched on, the levels of produced CO and CO_2, and consumed O_2 from around 30 ms onwards are considerably higher than for the case without. The details of late-time char conversion (where particle shrinkage effects that are ignored by the present model, cf. Sec. 2.3, will increasingly play a role) are not critical for the considered experimental campaign that mainly focused on devolatilization and ignition. Therefore the simulations are run up to 60 ms and then stopped. It is noted that at the end of the simulation that includes char conversion there still is a considerable amount of char and oxygen left (in a volume-averaged sense), which leads to further char conversion if the simulation is run longer. However, this process (accompanied by annealing reactions) is very slow possibly because a) the conversion/annealing reactions themselves are slow and/or b) despite the presence of elevated levels of O_2 at the particle surface there is no oxygen in the particle core that could convert the char, see Fig. 2 (right, 50 ms). This can be further examined by investigating axial profiles of temperature and main chemical species along the centerline inside the particle and in its proximate vicinity at selected time instants as shown in Fig. 4. At 29.5 ms the onset of homogeneous ignition can be recognized, as the gas temperature reaches ≈1900 K at $x/r_p = 8$ and some OH starts to form at that location. Afterwards both the peak temperature and OH mass fraction rapidly propagate towards the particle surface, reaching a stand-off distance of about $1…2d_p$ at 29.6 ms. At this time a significant amount of the reference coals has been consumed (especially in the outer layers of the particle where Y_{COAL} is already zero) to form the light volatile gases, the heavy tars ($Y_{TAR,max} > 30\%$ inside the particle) and the char that already represents more than 60% of the particle mass. At 35 ms the reference coals have been fully depleted and the consequent drop in the release of volatile matter, causes the (near-) extinction behavior observed in Fig. 2. Moreover, the absence of an intense convective flux from the particle after the end of devolatilization now allows for oxygen to diffuse inside the particle, as the increased levels of Y_{O_2} in its outer layer suggest. The presence of oxygen triggers the conversion of the char, which is responsible for the temperature increase observed at 50 ms, this time directly at the particle surface. The oxidation of the char occurs in the outer layers of the particle where both char and oxygen are consumed. As a consequence, oxygen cannot penetrate inside the core of the particle, which is mostly occupied by the char, that is therefore not further decomposed until the end of the simulation. Hence, in the inner particle region char conversion is diffusion-limited, since it is prevented by the lack of oxygen. The outer layers of the particle, however, still contain a substantial amount of oxygen, which should promote the conversion of the residual char. Yet, the significant amount of char present in that region, is consumed only slowly due to the slow kinetics of the char conversion/annealing reactions. The presence of both diffusion- and kinetically-limited char conversion at different locations inside the particle leads to the persisting volume-averaged char mass fraction at 60 ms that was discussed in the context of Fig. 3.

Figure 5 shows the time evolution of the maximum gas and particle temperatures, mass release rate and released mass, as well as the volume-averaged particle conversion, porosity and tortuosity for the two mixtures balanced with N_2. As the particle heats up, the mass release increases slowly, becoming significant only at around 20 ms. A drop in the release rate $\dot{m}$ after 20 ms can be observed for both mixtures and coincides with the full consumption of reference coals COAL2 and

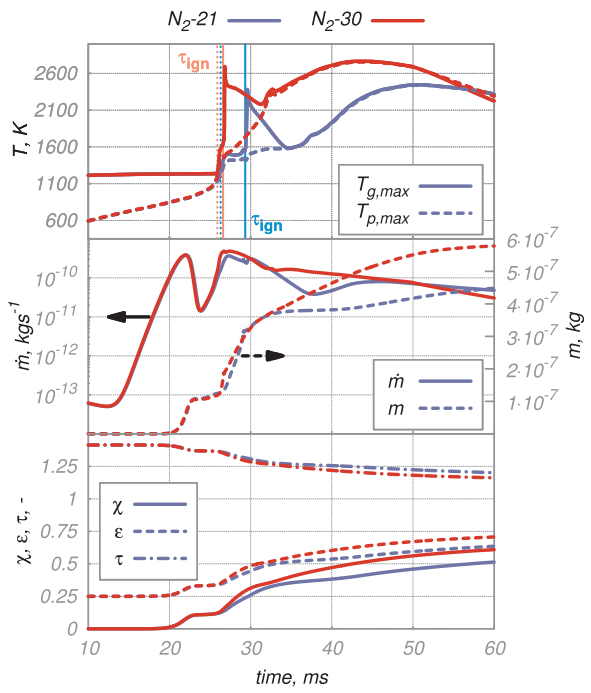

Fig. 5. Temporal evolution of the maximum gas and particle temperature (top), particle mass release rate and released mass (middle) and volume-averaged conversion, porosity and tortuosity of the particle (bottom). A comparison of the two gas mixtures balanced with N_2 is shown. Vertical dotted and solid lines represent the ignition delay times evaluated by criteria based on the first increase of T_{max} and its maximum temporal gradient, respectively. (For interpretation of the references to color in this figure, the reader is referred to the web version of this article.).

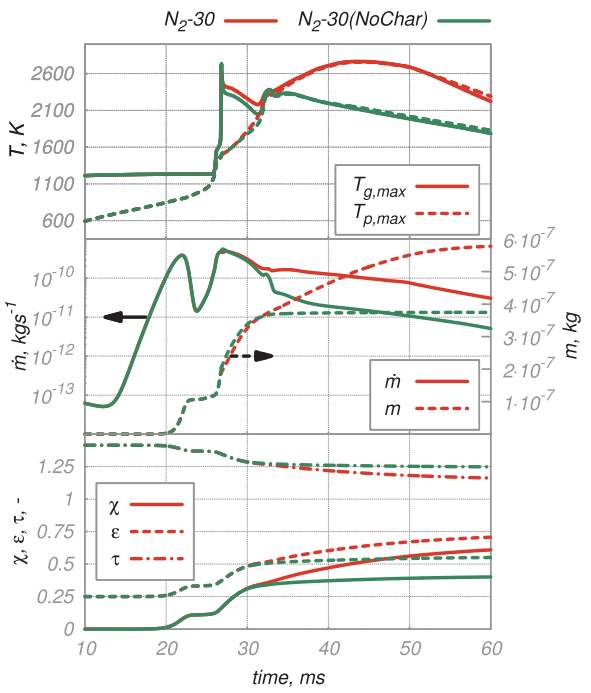

Fig. 6. Temporal evolution of the maximum gas and particle temperature (top), particle mass release rate and released mass (middle) and volume-averaged conversion, porosity and tortuosity of the particle (bottom). A comparison of case N_2-30 with a case that exhibits the particle to the identical gas environment N_2-30, but with char conversion switched off is shown. (For interpretation of the references to color in this figure, the reader is referred to the web version of this article.).

COAL3 as shown in Fig. 3. Observing the gas temperature profiles the ignition behavior is affected by the oxygen concentration. For case N_2-30 the onset of ignition is sudden and unique, whereas the mixture with 21% O_2 shows a two-stage ignition process with a temperature plateau between 26 and 29 ms, which corresponds to the final conversion period of COAL1.

After ignition, the gas temperature increases up to a peak value which is higher for the mixture containing more O_2 and, in general, for the mixtures balanced with N_2 rather than CO_2 (not shown for brevity). After reaching the peak gas temperature the volatile flame cools down, whereas the particle heats up until the temperature of the two phases is equilibrated (at 32 ms for case N_2-30 and 35 ms for N_2-21, see Fig. 5 (top)). Thereafter, the heat release resulting first from the combustion of the residual volatiles and then from char reactions increases the temperature of the gas phase in the immediate vicinity of the particle, and of the particle itself. Hence, the temperatures of the two phases stay in equilibrium, first increasing and then decreasing again at late times. The late time behavior of the mass release rate and released mass in Fig. 5 (middle) show a continuous decrease of the mass release rate and almost constant values of the released mass towards the end of the simulation. Figure 5 (bottom) shows the temporal evolution of the coal conversion χ which, as defined in Eq. (19), relates the mass released from the coal particle, Fig. 5 (middle), to the initial particle mass. Only limited extents of particle conversion are obtained towards the end of the simulation, around 50% for case N_2-21 and 60% for case N_2-30. The particle porosity and tortuosity follow their assumed linear relationships with particle conversion, Eqs. (20) and (22), therefore they can influence particle burning mainly by means of their initial value. For example reducing the initial porosity from 25% to 10% of the particle volume leads to an increase in the ignition delay time of the 'N_2-21' mixture by 12% (not shown), as the augmented presence of solid matter increases the thermal inertia of the particle, which slows down the pyrolysis process. To confirm that the late time behavior discussed in Fig. 5 is indeed caused by char conversion, Fig. 6 shows a comparison of the same quantities with and without char conversion for case $N_2 - 30$, where more char conversion happens than for case $N_2 - 21$. As can be seen from the profiles up to 27 ms, the cases with and without char conversion completely overlap, so the observed behavior is solely caused by pyrolysis. Between 27 and 33 ms (after ignition) small, but non-zero differences between the profiles can be observed, where small levels of char conversion seem to cause slight deviations from the pure pyrolysis profiles. From 33 ms onwards char conversion becomes significant and all quantities begin to deviate strongly. As a result, the case with char conversion shows significantly higher temperatures, more released mass, higher final particle conversion and porosity and lower final particle tortuosity than the case that neglects char reactions. Fig. 7 shows the ignition delay time τ_{ign} predicted by the numerical simulations along with the experimental measurements, for each of the conditions presented in Tab. 4. The experimental values of τ_{ign} result from the acquisition of the CH* chemiluminescence signal. In Tufano et al. [34] different ways of extracting ignition delay times from numerical simulations (based on species CH, OH and temperature) were compared and no significant influence of the chosen extraction method on τ_{ign} was found, similarly to what was found by Evans et al. [55] for autoigniting ethylene flames fed by hot air. The fact that the extraction criterion for ignition delay did not make any difference in [34] was probably related to the use of a single-step pyrolysis model, which results in monotonous temporal trends of the volatile release rate and combustion quantities. In contrast, the complex pyrolysis model employed here leads to non-monotonous profiles with one and two-step ignition scenarios as the ones shown in Fig. 5 and 6. As a consequence, different methods of extracting ignition delay times may give different results. Here, we compare τ_{ign} extracted from the maximum (overall) gas temperature to τ_{ign} extracted from the maximum temporal gradient of gas temperature (which may differ from case to case, if multi-stage ignition occurs). The

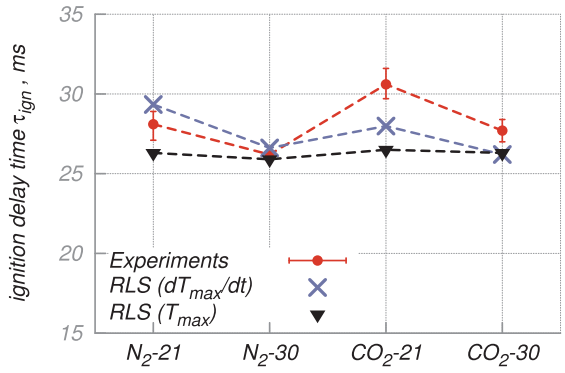

Fig. 7. Ignition delay times measured in [2] and extracted from the RLS based on T_{max} (triangles) or from its gradient (crosses). Vertical bars represent 98% confidence statistical error in the experiments. (For interpretation of the references to color in this figure, the reader is referred to the web version of this article.).

first criterion, indicated as 'T_{max}' in the legend of Fig. 7, evaluates the ignition delay time as the instant of the first increase of T_{max} from its base value (vertical dotted-lines in Fig. 5). The second criterion, indicated as 'dT_{max}/dt' in the legend of Fig. 7, defines τ_{ign} to lie at the interception of a line tangent to the (overall) maximum temporal gradient, with a horizontal line at the base value of T_{max} (vertical solid-lines in Fig. 5). In Fig. 7 it can be observed that irrespective of the chosen extraction method the simulation captures the measured ignition delay times very well. The experimental trend of decreasing ignition delay time with increased O_2 for a fixed balance gas is also captured by all simulations and the two extraction criteria, albeit this is more difficult to observe for the T_{max} criterion. However, the measured trend of increased ignition delay when changing from N_2 balance gas to CO_2 for a fixed oxygen concentration is only captured by the T_{max} criterion, whereas a slightly shorter τ_{ign} for CO_2 with 21% oxygen is found when using the temperature gradient criterion. We have verified that pure homogeneous gas phase kinetics and thermodynamics actually slightly increase the ignition delay times for CO_2. As a matter of fact, the higher specific heat of CO_2 decreases the gas temperature delaying ignition in homogeneous mixtures. Moreover, increased levels of CO_2 have a chemical effect of depleting H radicals throughthe reverse reaction of CO oxidation ($H + CO_2 \rightarrow OH + CO$), as was also considered in [27]. In our case, the heterogeneous chemistry of product release from the particle and the fuel/oxidizer mixing under strain partially hide these effects. Overall, it needs to be stated that the present detailed simulations provide a good representation of the experimental ignition delay, but since the predicted ignition delay times are all fairly similar, the trends with changing gas mixture -which are also small in the experiments- are difficult to corroborate for the selected set of cases.

5. Conclusions

A multi-step approach for heterogeneous kinetics coupled to detailed homogeneous chemistry is applied to fully-resolved simulations of single coal particle ignition and combustion in four different hot gas environments representing well-defined laminar flow experiments for the first time. A comprehensive model description is introduced for the particle interior, where a time-evolving porosity and tortuosity govern the particle internal fluid flow of gas formed during the thermal degradation of the coal. The model dynamically predicts the mass release rate and composition of species released from the particle by linear combination of a set of reference coals. The ignition sequence is investigated and shows a dependency of the particle burning behavior on the oxygen content in the surrounding gas. In the presence of lower oxygen concentrations, two-stage ignition phenomena are observed. The complex composition predicted by the porous-media model is analyzed and char conversion effects are discussed. Heterogeneous reactions result in considerably higher temperatures, enhanced mass release, and larger particle conversion along with a higher value of the final porosity. Slight deviations from the pure pyrolysis profiles are also found during the last stage of devolatilization, if char reactions are included. The predicted ignition delay times are in very good agreement with the experimental measurements, even though the complex profiles of the combustion quantities predicted by the detailed pyrolysis model lead to a mild dependence of the ignition delay time on the extraction method.

Acknowledgements

We acknowledge financial support by DFG (*Multi-Dimensional Flamelet Modeling for LES of Pulverized Coal Flames*, project numbers KR3684/8-2, KE1751/3-2, HA4367/3-2) and computational resources by HLRS Stuttgart.

Appendix A. Supplementary data

Supplementary data associated with this article can be found, in the online version, at https://doi.org/10.1016/j.fuel.2018.11.139.

References

[1] Hwang SM, Kurose R, Akamatsu F, Tsuji H, Makino H, Katsuki M. Energy Fuels 2005;19:382–92.
[2] Molina A, Shaddix CR. Proc Combust Inst 2007;31:1905–12.
[3] Balusamy S, Kamal MM, Lowe SM, Tian B, Gao Y, Hochgreb S. Exp Fluids 2015;56:108.
[4] Vorobiev N, Geier M, Schiemann M, Scherer V. Fuel Process Technol 2016;151:155–65.
[5] Köser J, Becker LG, Gossmann A-K, Böhm B, Dreizler A. Proc Combust Inst 2017;36:2103–11.
[6] Kurose R, Makino H. Combust Flame 2003;135:1–16.
[7] Yamamoto K, Murota T, Okazaki T, Taniguchi M. Proc Combust Inst 2011;33:1771–8.
[8] Pedel J, Thornock J, Smith P. Combust Flame 2013;160:1112.
[9] Stein OT, Olenik G, Kronenburg A, Marincola F, Franchetti B, Kempf AM, Ghiani M, Vascellari M, Hasse C. Flow Turbul Combust 2013;90:859.
[10] Chen L, Ghoniem AF. Energy Fuels 2012;26:4783–98.
[11] Olenik G, Stein OT, Kronenburg A. Proc Combust Inst 2015;35:2819.
[12] Rabacal M, Franchetti B, Cavallo-Marincola F, Proch F, Costa M, Hasse C, Kempf AM. Proc Combust Inst 2015;35:3609–17.
[13] Muto M, Watanabe H, Kurose R, Komori S, Balusamy S, Hochgreb S. Fuel 2015;142:152–63.
[14] Rieth M, Proch F, Rabacal M, Franchetti BM, Marincola FC, Kempf AM. Combust Flame 2016;173:39–56.
[15] Wen X, Luo K, Luo Y, Kassem HI, Jin H, Fan J. Appl Energy 2016;183:1086–97.
[16] Wan K, Xia J, Wang Z, Pourkashanian M, Cen K. Flow Turbul Combust 2017;99:531–50.
[17] Knappstein R, Kuenne G, Becker LG, di Mare F, Sadiki A, Dreizler A, Janicka J. Flow Turbul Combust 2018;101:895–926.
[18] Messig D, Vascellari M, Hasse C. Combust Theor Model 2017;21:700.
[19] Wen X, Luo K, Jin H, Fan J. Fuel 2017;195:232–42.
[20] Knappstein R, Kuenne G, Meier T, Sadiki A, Janicka J. Fuel 2017;201:39–52.
[21] Brosh T, Patel D, Wacks D, Chakraborty N. Fuel 2015;145:50–62.
[22] Krüger J, Haugen NEL, Løvås T. Combust Flame 2017;185:160–72.
[23] Muto M, Yuasa K, Kurose R. Fuel 2017;190:136–44.
[24] Rieth M, Kempf AM, Kronenburg A, Stein OT. Fuel 2018;212:364–74.
[25] Luo K, Wang H, Fan J, Yi F. Energy Fuels 2012;26:6128–36.
[26] Hara T, Muto M, Kitano T, Kurose R, Komori S. Combust Flame 2015;162:4391–407.
[27] Farazi S, Attili A, Kang S, Pitsch H. Numerical study of coal particle ignition in air and oxy-atmosphere. Proc Combust Inst 2018;37 available online,https://www.sciencedirect.com/science/article/pii/S1540748918304206.
[28] Zhang W, Watanabe H, Kitagawa T. Adv Powder Technol 2017;28:2893–902.
[29] McConnell J, Goshayeshi B, Sutherland JC. Fuel 2017;201:53–64.
[30] Nikrityuk P, Gräbner M, Kestel M, Meyer B. Fuel 2013;114:88–98.
[31] Farazi S, Sadr M, Kang S, Schiemann M, Vorobiev N, Scherer V, Pitsch H. Fuel 2017;201:15–28.
[32] Sayadi T, Farazi S, Kang S, Pitsch H. Fuel 2017;199:289–98.
[33] Vascellari M, Xu H, Hasse C. Proc Combust Inst 2013;34:2445.
[34] Tufano GL, Stein OT, Kronenburg A, Frassoldati A, Faravelli T, Deng L, Kempf AM, Vascellari M, Hasse C. Fuel 2016;186:285–92.
[35] Vascellari M, Tufano GL, Stein OT, Kronenburg A, Kempf AM, Scholtissek A, Hasse C. Fuel 2017;201:29–38.
[36] Tufano GL, Stein OT, Wang B, Kronenburg A, Rieth M, Kempf AM. Fuel

2018;229:262–9.
[37] Tufano GL, Stein OT, Wang B, Kronenburg A, Rieth M, Kempf AM. Fuel 2018;234:723–31.
[38] Gentile G, Debiagi PEA, Cuoci A, Frassoldati A, Ranzi E, Faravelli T. Chem Eng J 2017;321:458–73.
[39] Maffei T, Khatami R, Pierucci S, Faravelli T, Ranzi E, Levendis YA. Combust Flame 2013;160:2559–72.
[40] Maffei T, Gentile G, Rebughini S, Bracconi M, Manelli F, Lipp S, Cuoci A, Maestri M. Chem Eng J 2016;283:1392–404.
[41] Hassanaly M, Koo H, Lietz CF, Chong ST, Raman V. Comput Fluids 2018;162:11–25.
[42] Gronli MG, Melaaen MC. Energy Fuels 2000;14:791–800.
[43] Coffee T, Heimerl J. Combust Flame 1981;43:273–89.
[44] Ranzi E, Faravelli T, Manenti F. Geem KMV, editor. Thermochemical Process Engineering, volume 49 of Advances in Chemical Engineering. Academic Press; 2016. p. 1–94.
[45] Curtiss C, Hirschfelder J. J Chem Phys 1949;17:550–5.
[46] Cheng P. AIAA J 1964;2:1662–4.
[47] Modest MF. Radiative Heat Transfer. Academic Press; 2003.
[48] Burcat A, Rusic B. Third millenium ideal gas and condensed phase thermochemical database for combustion (with update from active thermochemical tables), Argonne National Laboratory, report No. ANL-05/20; 2005.
[49] Cuoci A, Frassoldati A, Faravelli T, Ranzi E. Comp Phys Communic 2015;192:237–64.
[50] Paulsen AD, Mettler MS, Dauenhauer PJ. Energy Fuels 2013;27:2126–34.
[51] Sommariva S, Maffei T, Migliavacca G, Faravelli T, Ranzi E. Fuel 2010;89:318–28.
[52] Ranzi E, Frassoldati A, Grana R, Cuoci A, Faravelli T, Kelley A, Law C. Prog Energy Combust Sci 2012;38:468–501.
[53] CRECK modeling group.http://CRECKmodeling.chem.polimi.it; 2018.
[54] Stagni A, Frassoldati A, Cuoci A, Faravelli T, Ranzi E. Combust Flame 2016;163:382–93.
[55] Evans MJ, Medwell PR, Tian ZF, Frassoldati A, Cuoci A, Stagni A. AIAA J 2016;54:3255–64.